Predictability of Extratropical Cyclones: The Influence of Initial Condition and Model Uncertainties

HONGYAN ZHU AND ALAN THORPE

Department of Meteorology, University of Reading, Reading, United Kingdom

(Manuscript received 23 February 2005, in final form 20 September 2005)

ABSTRACT

Errors in numerical weather forecasts can be attributed to two causes: deficiencies in the modeling system and inaccurate initial conditions. Understanding of the characteristics of the growth of forecast spread related to model uncertainty is less developed than that for initial condition uncertainty. In this research, the authors aim to construct a theoretical basis for describing such forecast error growth resulting from model uncertainty using mostly an empirical modeling approach. Primitive equation models with different vertical discretization and different horizontal resolutions are used to investigate the impacts of model uncertainties on the predictability of extratropical cyclones. Three sets of initial perturbations related to an upper-level trigger, with slightly different amplitudes, are designed for representing the situation when the initial condition uncertainty leads to significant forecast error growth.

Forecast error growth is here estimated by following the properties of a developing cyclone in the simulations. Generally, there are three phases for forecast error growth in the experiments with initial condition and model uncertainties. For the experiments with the structured initial condition uncertainties, the errors grow rapidly at the earlier transient stage, with the growth rate well above the fastest growing normal mode. Afterward the error grows exponentially at approximately the same growth rate as the cyclone, followed by a saturation period, when the growth rate starts to decline. For the experiments with the model uncertainties, the forecast errors are initially zero and increase as time to a power of μ, which is between 0.5 and 3 depending on the strength of the cyclone at the time the simulation is initiated. After a certain time interval, the exponential growth phase and saturation period start as in the initial error experiments. Starting an integration with a stronger initial cyclone, the forecast error associated with the model uncertainty takes a shorter time to reach the exponential growth period and the forecast error grows more rapidly initially with a smaller value of μ. Also, when the initial cyclone is strong enough, then the exponential growth phase may only last for a very short time.

1. Introduction

Factors that contribute to uncertainty in numerical weather prediction are: 1) uncertainty in the physical laws governing atmospheric motions, notably in the numerical approximations used for their solution and the parameterizations of the unresolved motions; 2) uncertainty in the forecast initial conditions arising from systematic and random errors in the observations, inhomogeneity in the spatial and temporal coverage of observations, representativeness a given observation system to the spatial and temporal scales resolved by the forecast model, errors in background forecast and approximations in data assimilation systems (Thompson 1957). Factors 1 and 2 are referred to as model uncertainty and initial condition uncertainty, respectively. It has been suggested that at short range, the improvements in the initial condition are likely to be more effective, while at a more extended range, improvements in the model play a greater role in improving the performance of the forecast system (Lorenz 1989).

Ever since Lorenz (1963) discovered that weather prediction is a chaotic system, and therefore sensitive to the initial conditions, attention has focused on the initial conditions as the primary contributor to forecast error. The current state of the atmosphere can only be known to a certain tolerance, which depends on the quantity and quality of available observations. A small

Corresponding author address: Dr. Hongyan Zhu, Dept. of Meteorology, University of Reading, Earley Gate, P.O. Box 243, Reading, United Kingdom.
E-mail: hongyan.zhu@reading.ac.uk

initial uncertainty results, according to the theory, in a near-total loss of skill after a period of between 7 and 14 days.

Weather forecast centers have made considerable efforts over the past several years to combating the effects of initial condition uncertainty. This includes reducing the uncertainty by improvements in the observational system, such as with the availability of a larger number of satellite measurements. The main modeling innovation is ensemble forecasting, where an ensemble of initial conditions, within some tolerance of the observed state, is run forward with the model to get an impression of the likely range of future states (Toth and Kalnay 1993; Molteni et al. 1996; Palmer 2000). Perturbations are carefully chosen to capture the direction of fastest error growth (Buizza et al. 1999).

In addition to uncertainty in initial conditions, the accuracy of weather and climate forecasts are influenced by our ability to represent computationally the full equations that govern weather. Forecast errors can be contributed to both of random and systematic errors in model performance. One kind of forecast error is caused by the inevitable uncertainties in the parameterized representation of unresolved processes as discussed by Palmer (1999). Another kind of systematic error of weather predictions is due to the imperfect numerical methods to solve the partial difference equations. For example, there are at least four kinds of common vertical discretization coordinates (Eta, generic hybrid, isentropic-sigma hybrid, and sigma), which have been used in weather forecast models. They all have primary advantages and limitations. Even for the same vertical coordinate, there are different ways to distribute the different variables on the vertical grid. One vertical grid is the Charney–Phillips grid (referred as CP grid), developed by Charney and Phillips (1953). Arakawa and Moorthi (1988, hereafter AM88) pointed out that the most straightforward way to maintain the conservation of quasigeostrophic potential vorticity is to use a CP grid model. CP-grid staggering in the vertical has been one part of the New Dynamics Package, which was implemented on 7 August 2002 in the U.K. Met Office Numerical Weather Prediction model (*NWP Gazette*, June 2002, U.K. Met Office). Lorenz (1960) deviated from the CP grid by introducing a new grid, referred to as the L grid. Arakawa and Konor (1996, hereafter AK96) show that for the L grid, a computational mode arises because of the extra freedom available in the temperature field and typically appears as an oscillation of potential temperature. Even though the L grid has been shown to lead to a computational mode in the vertical distribution of potential temperature (Tokioka 1978; AM88; Cullen et al. 1997; Hollingsworth 1995; AK96), it has been adopted by existing primitive equation models [e.g., fifth-generation Pennsylvania State University–National Center for Atmospheric Research (NCAR) mesoscale model (MM5); Arakawa and Lamb 1997; Simmons and Burridge 1981; Arakawa and Suarez 1983]. The L grid has certain desirable attributes; for example, it enables the total energy, the mean potential temperature, and the variance of the potential temperature to be conserved under adiabatic and frictionless processes (Arakawa 1972; Arakawa and Lamb 1977; Arakawa and Suarez 1983).

Some indications of the relative importance of the two sources of forecast error can be deduced from the work of Downton and Bell (1988) and Richardson (1997), who compared forecasts given by the U.K. Met Office (UKMO) and the European Centre for Medium-Range Weather Forecasts (ECMWF) forecasting systems. In these studies, substantial forecast differences between the ECMWF and the UKMO operational forecasts could mostly be traced to differences between the two operational analyses, rather than between forecast models. On the other hand, recent results from Harrison et al. (1999) indicate that the impact of model uncertainties on forecast error cannot be ignored.

A study by Orrell et al. (2001), claimed that the component of forecast error due to state-dependent model error tends to grow initially as the square root of forecast time, and provides a major source of error out to three days. They suggested that model error plays a major role in contributing to weather forecast error.

Power-law behavior associated with the dynamics of model error also has been studied by Nicolis (2003) and Vannitsem and Toth (2002). Their analyses of a simplified mathematical model and the low-order Lorenz system indicated that the mean square error closely follows a quadratic evolution for short times.

The understanding of the characteristics of the growth of forecast spread related to model uncertainty is less developed than that for initial condition uncertainty. In an operational forecast system, it is not easy to separate the predictability problem into a component associated with initial condition uncertainty and a component associated with model uncertainty because of the data assimilation process. In this research we aim to construct a theoretical basis for describing model uncertainty forecast "error" growth using mostly an empirical modeling approach that is able to separate the two sources of forecast error so as to compare the forecast error growth associated with the model and initial condition uncertainties. An initial baroclinic jet basic state is constructed with a balanced three-dimensional perturbation to trigger a baroclinic wave

development. Three sets of initial perturbations related to the upper-level trigger, with slightly different amplitudes, are designed to represent the initial condition uncertainty. Since models with CP grids and L grids are both popular for current weather forecast models, model simulations with these two different grids are used to investigate the impacts of model uncertainty. Also model forecasts with different grid resolutions are studied here for the investigation of the model uncertainty because different numerical forecast systems have different resolution. Furthermore we investigate the sensitivity of forecast error growth, associated with model uncertainty, to the intensity of the initial cyclone.

For simplicity, the numerical calculation carried on in this study is dry simulation and no other physical processes, except of horizontal diffusion, are included. The model description and experiment design are described in section 2. The main results are presented in section 3 and the discussion and summaries are given in section 4.

2. Model description and experiment design

a. Model equations

The basic equations on the L grid and CP grid are detailed in Zhu et al. (2001) and Zhu and Smith (2003). The model is based on the three-dimensional hydrostatic primitive equations in sigma-coordinates (x, y, σ) on an f plane centered at 50°N, where x and y are in the zonal and meridional directions, respectively, and

$$\sigma = \frac{p - p_{\text{top}}}{p_s - p_{\text{top}}} = \frac{p - p_{\text{top}}}{p^*}, \tag{1}$$

$p^* = p_s - p_{\text{top}}$, and p_s and p_{top} are the surface and top pressures with p_{top} a constant, taken here to be 50 hPa. The upper and lower boundary conditions require that $\dot{\sigma} = 0$ at $\sigma = 0$ and $\sigma = 1$, where $\dot{\sigma} = D\sigma/Dt$ and D/Dt is the material derivative.

The zonal and meridional momentum equations and the hydrostatic equation are

$$\frac{\partial p^* u}{\partial t} = -\left(\frac{\partial p^* u^2}{\partial x} + \frac{\partial p^* u v}{\partial y}\right) - \frac{\partial p^* u \dot{\sigma}}{\partial \sigma} + p^*\left(fv - \frac{RT\sigma}{p}\frac{\partial p^*}{\partial x} - \frac{\partial \Phi}{\partial x}\right), \tag{2}$$

$$\frac{\partial p^* v}{\partial t} = -\left(\frac{\partial p^* u v}{\partial x} + \frac{\partial p^* v^2}{\partial y}\right) - \frac{\partial p^* v \dot{\sigma}}{\partial \sigma} - p^*\left(fu - \frac{RT\sigma}{p}\frac{\partial p^*}{\partial y} - \frac{\partial \Phi}{\partial y}\right), \tag{3}$$

$$\frac{\partial \Phi}{\partial \sigma} = -\frac{RTp^*}{p}, \tag{4}$$

where u and v are the velocity components in the x and y directions, f is the Coriolis parameter, R is the specific gas constant for dry air, $\kappa = R/c_p$, c_p is the specific heat of dry air, θ is the potential temperature, and Φ is the geopotential. The surface pressure tendency equation, derived from the continuity equation and boundary conditions is

$$\frac{\partial p^*}{\partial t} = -\int_0^1 \left[\frac{\partial (p^* u)}{\partial x} + \frac{\partial (p^* v)}{\partial y}\right] d\sigma \tag{5}$$

and $\dot{\sigma}$ is given by

$$\dot{\sigma} = -\frac{1}{p^*}\int_0^\sigma \left[\frac{\partial (p^* u)}{\partial x} + \frac{\partial (p^* v)}{\partial y}\right] d\sigma + \frac{\sigma}{p^*}\int_0^1 \left[\frac{\partial (p^* u)}{\partial x} + \frac{\partial (p^* v)}{\partial y}\right] d\sigma. \tag{6}$$

The thermodynamic equation is

$$c_p \frac{\partial p^* T}{\partial t} = -c_p\left(\frac{\partial p^* u T}{\partial x} + \frac{\partial p^* v T}{\partial y}\right) - c_p \frac{\partial p^* \dot{\sigma} T}{\partial \sigma} + p^* \alpha \omega \tag{7}$$

or

$$\frac{\partial p^* \theta}{\partial t} = -\left(\frac{\partial p^* u \theta}{\partial x} + \frac{\partial p^* v \theta}{\partial y}\right) - \frac{\partial p^* \dot{\sigma} \theta}{\partial \sigma}, \tag{8}$$

where α is the specific volume, ω is the vertical p velocity, and

$$T = \left(\frac{p}{p_o}\right)^\kappa \theta = \frac{(p^*\sigma + p_{\text{top}})^\kappa}{p_o^\kappa}\theta, \tag{9}$$

where $p_o = 1000$ hPa.

b. The vertical differencing in the L grid and CP grid model

The vertical differencing in the L grid model is based on the method proposed by Arakawa and Suarez (1983), which guarantees that the variance of θ is conserved. In the CP grid model, we adopt the vertically discrete equations and hydrostatic equation of AK96, which are designed to satisfy the constraints (i) and (ii) advocated by Arakawa and Lamb (1977), mainly that the total energy is conserved under adiabatic frictionless processes and that there is no circulation generated along a contour of surface topography.

The model is divided vertically into 16 equally deep layers. In the CP grid model, the horizontal velocity, and geopotential are calculated at full levels, while the potential temperature and vertical velocity, $\dot{\sigma}$, are stored at half levels as indicated in Fig. 1a. In the L grid model, all the dependent variables such as horizontal

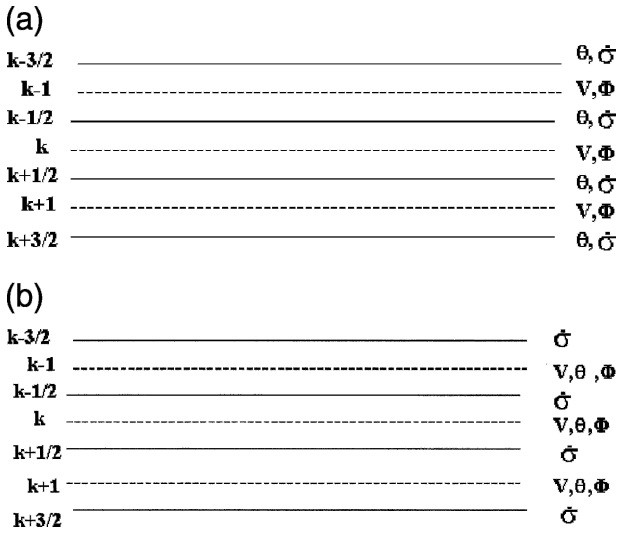

FIG. 1. Configuration of σ levels in the (a) CP grid and (b) L grid models.

velocity, potential temperature, and geopotential, are defined in the middle of each layer (full levels in the Fig. 1b), and $\dot{\sigma}$ is staggered.

c. Boundary conditions and subgrid-scale diffusion

The calculations are carried out in a zonal channel with rigid walls at $y = 0$ and $y = Y$ and periodic boundary conditions at $x = 0$ and $x = X$. The computational grid size is 200×90, and the grid resolution is 90 km.

A fourth-order horizontal diffusion term $D_4 = -k_1\nabla_h^4\chi$ is added to all prognostic equations with a diffusion coefficient $k_1 = 0.0008\Delta^4$, where ∇_h^2 is the horizontal Laplacian operator and Δ is the horizontal grid spacing. This subgrid-scale diffusion is used to filter out the energy in high frequency waves. At the boundaries, a second-order diffusion term $D_2 = -k_2\nabla_h^2\chi$ is applied with $k_2 = 0.0008\Delta^2$.

d. Initial condition

The initial condition is similar to that used in the paper by Tan et al. (2004), in which an idealized two-dimensional baroclinic jet is combined with a balanced three-dimensional perturbation for a rapid baroclinic wave development. The initial baroclinic jet basic state is shown in Fig. 2a, which has a jet speed maximum of 55 m s^{-1} at about 8 km height. The tropopause is indicated by the heavy black dashed line in Fig. 2a, where the potential vorticity (PV) is equal to 1.5 PV units (PVU; 1 PVU = 10^{-6} m^2 K kg^{-1} s^{-1}). The baroclinic jet is designed by specifying the position of the tropopause with a low PV value in the troposphere, and high PV value in the stratosphere, as in Rotunno et al. (1994).

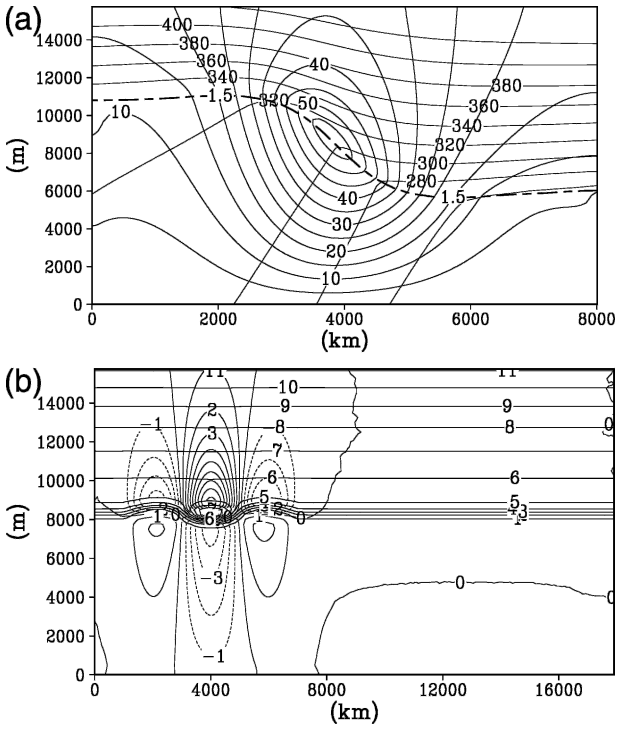

FIG. 2. (a) Vertical cross section of initial potential temperature (gray lines) and zonal velocity (black lines) for the initial basic-state jet. The heavy black dashed line denotes the location of the tropopause where potential vorticity is 1.5 PVU. The horizontal axis is oriented south–north and the vertical axis is the height. (b) Vertical cross section of the initial PV field (PVU, black lines) and the potential temperature anomaly (K, gray lines). The horizontal axis is oriented west–east and the vertical axis is the height.

As in Tan et al. (2004), an upper-level PV perturbation (PV′) is added to the basic stage to trigger rapid cyclone genesis. Similar to Rotunno and Bao (1996), the perturbation is proportional to the meridional gradient of the basic-state PV. Figure 2b shows that the PV perturbation is centered at $x_c = 4000$ km and at the height of tropopause. Related to the PV perturbation, there is positive potential temperature anomaly above the PV perturbation, and negative potential temperature anomaly below. For the control initial condition, the PV′ is defined as

$$\mathrm{PV}' = \frac{na^2}{a^2 + (x - x_c)^2}\frac{\partial Q}{\partial y}\sin\frac{\pi y}{y_L}\cos\frac{2\pi(x - x_c)}{x_L},$$
$$|x - x_c| < \frac{3x_L}{4}, \quad 3000\ \mathrm{km} < y < 5000\ \mathrm{km}, \tag{10}$$

where n is a parameter determining the amplitude of PV′, for example, $n_0 = -0.4 \times 10^6$ m, $a = 1.863 \times 10^6$ m, $y_L = 8 \times 10^6$ m, $x_L = 4 \times 10^6$ m; $\partial Q/\partial y$ is the

meridional basic-state potential vorticity gradient, where Q is the specified potential vorticity field associated with the zonally invariant baroclinic jet shown in Fig. 2a. The perturbed PV field is inverted to obtain the streamfunction and geopotential (and thus wind and temperature) fields using the PV inversion technique of Davis and Emanuel (1991).

To investigate the influence of the initial perturbation on the predictability of extratropical cyclone, the amplitude of the PV′ in Eq. (10) is increased or decreased by 25%. As a result, the maximum wind speed associated with the PV perturbation will increase or decrease by 0.5 m s^{-1} and the potential temperature will increase or decrease by 1 K. These changes have magnitudes typical of known observation errors. Therefore each of the three initial conditions could be considered as an equally probable estimate of the "true" initial state of the atmosphere.

e. Experiment design

Five experiments are carried out as detailed in Table 1. The first experiment is the calculation with CP grid and the control initial condition as shown in Fig. 2. Experiments 2 and 3 (hereafter Expt. 2 and Expt. 3, respectively) are based on the CP grid, with the amplitude of PV′ being increased or reduced by 25%. Expt. 4 has the same initial data as in Expt. 1, but applies the L grid in the vertical. Expt. 5 is the same as Expt. 1, except that the horizontal grid distance is 45 km, half of that in Expt. 1, but the number of grid points is doubled to keep the same domain size as Expt. 1. Expt. 1 is the control experiment, and Expts. 2 and 3, which have slightly different initial conditions, are compared with Expt. 1 to investigate the characteristics of forecast error growth arising from the initial uncertainties. Expt. 4 and Expt. 5 are designed with a different vertical grid and different horizontal resolution, respectively, for studying the role of model uncertainties on the forecast error growth.

TABLE 1. List of experiments described in this paper.

Expt.	n	Grid	Resolution
1	n_0	CP	90 km
2	$1.25 \times n_0$	CP	90 km
3	$0.75 \times n_0$	CP	90 km
4	n_0	L	90 km
5	n_0	CP	45 km

3. The calculations

a. Initial condition uncertainty

The evolution of the extratropical cyclone in Expt. 1 is shown in Fig. 3. The initial perturbation consists of a positive circular finite-amplitude PV anomaly located near the level of the tropopause (Fig. 2b), and after day 1, a weak surface cyclone starts to develop (Fig. 3a). At day 2, an obvious surface low pressure with a central value of 992 hPa and two anticyclones develop slightly to the east of the initial upper-level perturbation (Fig. 3b). At day 3, the primary cyclone further intensifies and the central surface pressure is about 976 hPa, with two anticyclones to the south (Fig. 3c). At day 4, the surface pressure minimum of the primary cyclone reaches 944 hPa, and a well-defined warm front and cold front develop with pronounced warm-air seclusion (Fig. 3d). At this time, downstream and upstream cyclones appear in the surface pressure field.

The primary cyclone's central surface pressure evolutions are compared in Fig. 4a for Expts. 1, 2, and 3, in which the initial PV′ have different amplitudes. The differences in the initial minimum central surface pressure of Expts. 2 and 3 are less than 1 hPa relative to Expt. 1. After 108 h, the central surface pressure is about 5 hPa deeper in Expt. 2, and 7 hPa shallower in Expt. 3 compared to Expt. 1.

The concept of a growth rate is useful to characterize the rate of development of a cyclone, or of forecast errors. The evolution evident in Fig. 4a has been the subject of dynamical theories for much of the twentieth century. The use of normal modes to describe baroclinic instability, following on from Eady (1949), provides one theory of growth whereby the cyclone perturbation increases exponentially in time at least for the period when its amplitude is small. Therefore, one way to model the rate of development, or growth rate, evident in Fig. 4a involves hypothesizing an exponential time dependence. This theory suggests that a cyclone growth rate in terms of the perturbation of the central surface pressure relative to the reference mean surface pressure, 1000 hPa, can be defined by

$$\lambda_{\delta P} = \frac{\ln\left(\frac{\delta P_{t+\delta t}}{\delta P_t}\right)}{\delta t}, \tag{11}$$

where δP (a measure of the intensity of the cyclone) is the absolute value of the difference of the central minimum surface pressure relative to the reference value, 1000 hPa, λ is the exponential growth rate, and δt is the time interval, here taken to be 1 h. This method of analysis has been used extensively, including for instance calculations of perturbation kinetic energy growth rate (e.g., Badger and Hoskins 2001).

Figure 4b shows the growth rate calculated by apply-

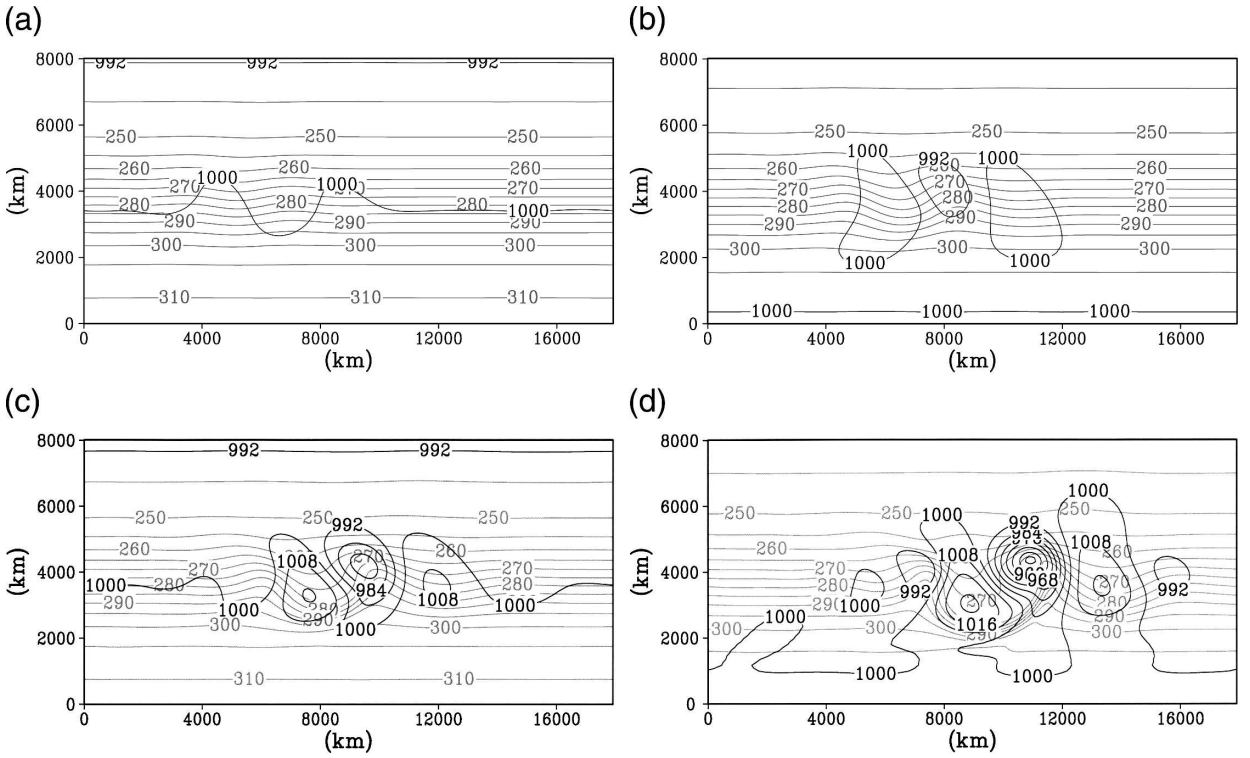

FIG. 3. Flow evolution for the numerical simulation of Expt. 1 at (a) day 1, (b) day 2, (c) day 3, and (d) day 4. The black solid lines are the contours of the surface pressure (contour interval 8 hPa) and gray solid lines represent the surface potential temperature with the interval of 5°C.

ing Eq. (11) to the cyclone evolution shown in Fig. 4a for Expts. 1, 2, and 3. For Expt. 1, during the period from 45 to 77 h, the vortex grows exponentially with the approximately constant growth rate of 8.0×10^{-6} s^{-1}, and therefore we refer to this as the exponential growth period. Before 45 h, the growth rate reaches a maximum value well above that of the most unstable normal mode, and following Farrell (1982, 1984) and Badger and Hoskins (2001), this transient period of the development of the cyclone is referred as the initial rapid growth period. After about 77 h, the cyclone intensification starts to slow down, and the growth rates starts to decline. This period is referred to as the saturation period. For the Expts. 2 and 3, in which the amplitude of the initial PV′ is slightly bigger and smaller, respectively, than that in Expt. 1, the normal mode growth rates are approximately the same as in Expt. 1. The exponential growth period in Expt. 2 starts at about 45 h and ends at 70 h, and that in Expt. 3 lasts longer than Expt. 1, starting at about 45 h and finishing at 85 h. It is clear that the calculation with larger amplitude initial PV perturbation has a larger growth rate during the initial rapid growth period, and the exponential growth period is shorter.

Farrell (1982) has given a conceptual explanation of the rapid growth phase based on a consideration of the quasigeostrophic potential vorticity of the perturbation. This is referred to as nonnormal mode growth and it relies on the changing spatial pattern of the PV perturbation that has been imposed at the initial time as a finite amplitude disturbance. The perturbation PV is simply advected by the basic zonal wind. The differential advection of the PV distribution by the zonal wind produces a perturbation that has wind and pressure fields that tilt against the shear. In contrast the longer-term sustained growth is due to the coupling of boundary Rossby waves leading to the emerging domination of the fastest growing normal-mode solution.

To measure the forecast error growth associated with initial condition uncertainty, Fig. 5a shows the central surface pressure difference of Expts. 2 and 3 from that of Expt. 1. At the initial time, the surface pressure perturbations relative to the control experiment are about 0.5 hPa in Expts. 2 and 3. The difference of the central surface pressure reaches the maximum of 7.8 hPa at 85 h, and 11 hPa at 90 h in Expts. 2 and 3, respectively.

Similar to the central surface pressure evolution itself, the forecast error growth of the central surface pressure associated with initial condition uncertainty also tends to be characterized by an early initial phase

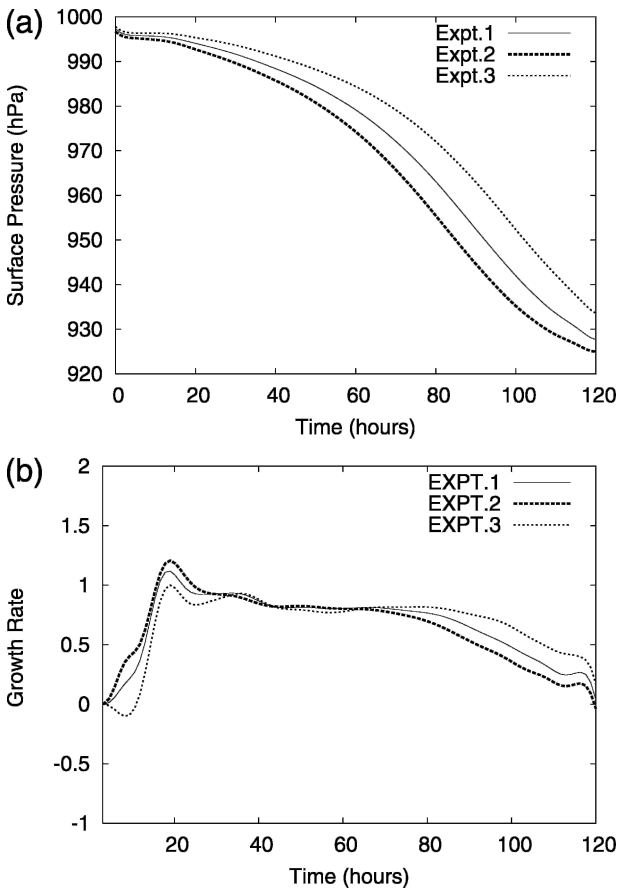

FIG. 4. (a) The central surface pressure (hPa) and (b) exponential growth rate ($\times 10^{-5}$ s^{-1}) evolution for Expts. 1, 2, and 3.

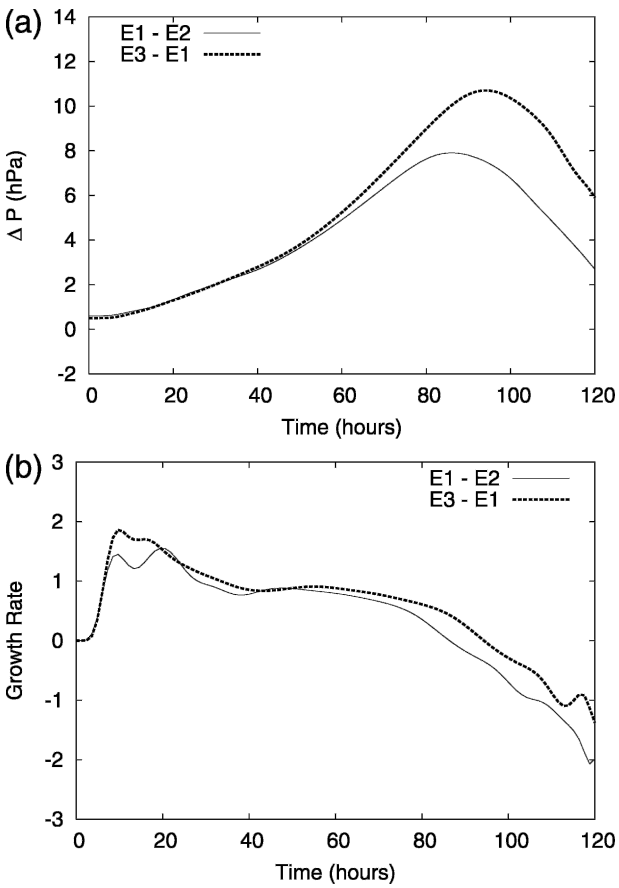

FIG. 5. (a) The central surface pressure difference (ΔP) of Expts. 2 and 3 from that of Expt. 1, and (b) error growth rate ($\times 10^{-5}$ s^{-1}) measured by the central surface pressure difference of Expts. 2 and 3 from that of Expt. 1.

of transient growth that exceeds that of the fastest growing normal mode, followed by an exponential growth period and then the saturation period. Figure 5b shows the exponential growth rate of the forecast error in terms of the difference of the central surface pressure between Expt. 1 and Expts. 2 and 3. Here we have supposed that the growth of differences between two forecasts, with slightly different initial conditions, is represented [by analogy with Eq. (11)] in the following way:

$$\lambda_{\Delta P} = \frac{\ln\left(\frac{\Delta P_{t+\delta t}}{\Delta P_t}\right)}{\delta t}, \tag{12}$$

where ΔP (a measure of the forecast error) is the absolute value of the difference between the minimum central surface pressure between two forecasts, that start from different initial conditions. Therefore, in this paper we use ΔP and δP to represent different measures of the central surface pressure perturbation. The latter, representing the difference of the central surface pressure relative to 1000 hPa, has been used to measure the intensity of the cyclone in Eq. (11).

After the initial rapid growth, the forecast errors (Fig. 5b) for Expts. 2 and 3 both start to grow exponentially at about 45 h, when the central surface pressure perturbation is about 2.5 hPa, with the approximately same growth rate as that of the cyclone itself (shown in Fig. 4b), 8×10^{-6} s^{-1} for Expt. 2, and 9×10^{-6} s^{-1} for Expt. 3. The similarity of the exponential growth rate of the cyclone itself and of initial condition uncertainties is well known. It occurs because forecast error perturbations, like any other perturbations, grow via baroclinic processes and so will have a characteristic exponential growth rate typical of such processes. This shows that over the lifetime of a cyclone it is important to have accurate initial conditions to be able to forecast cyclone development with sufficient skill. If it had been the case that error growth were much faster than that of the cyclone itself then the existing such forecast error would prevent skillful forecasts from being possible.

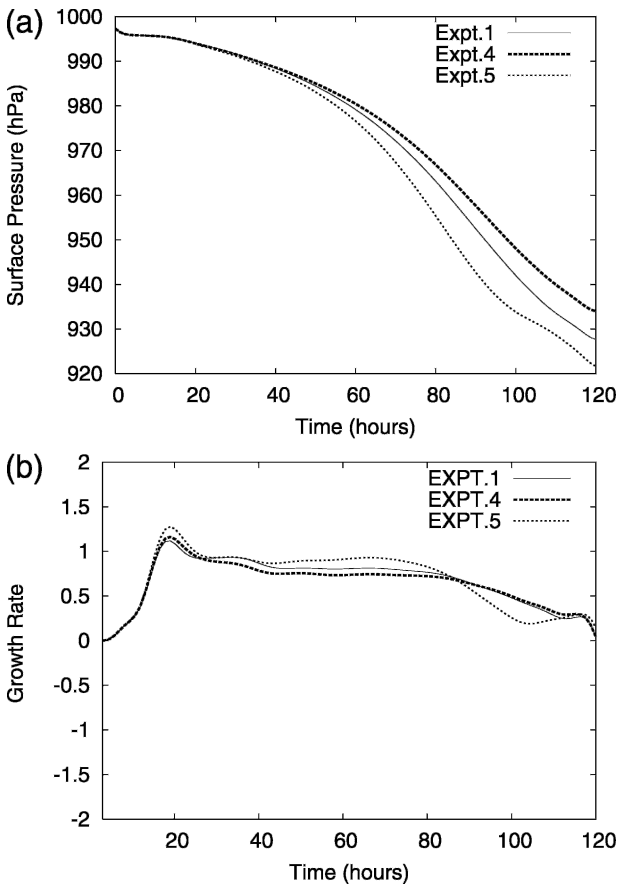

FIG. 6. (a) The central surface pressure (hPa) and (b) exponential growth rates, ($\times 10^{-5}$ s^{-1}) evolution for Expts. 1, 4, and 5.

During both the early initial transient growth phase and the normal mode growth phase, the error growth rate in Expt. 3 is slightly bigger than that in Expt. 2.

There are different ways to perturb the initial conditions, such as adding a structured perturbation as in this study, changing the position of the initial perturbation (cf. Takayabu 1991), changing the basic-state background flow (e.g., Wernli et al. 1998). Snyder et al. (2003) represented the initial condition uncertainties by adding a random small-scale perturbation. In their paper they found that the resulting perturbation energy decays for the first day, followed by amplification that becomes exponential for $t > 3$ days, and they attributed this initial decay to the dissipation in the model. Therefore, the transient period for the early initial phase with the initial condition uncertainties may not necessarily grow rapidly as in Expts. 2 and 3 depending on the way that the perturbation is structured.

b. Model uncertainties

To study the forecast error associated with model uncertainties, we compare the differences of Expt. 1 with Expts. 4 and 5, in which the model has different configurations, but the same initial condition as the control experiment.

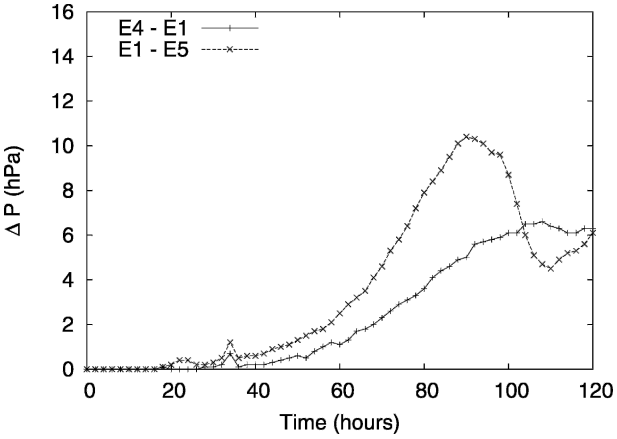

FIG. 7. The central surface pressure difference relative to Expt. 1, for Expts. 4 and 5.

Figure 6a compares the central minimum surface pressure for the three calculations of Expts. 1, 4, and 5. The initial stages of these three experiments are identical. Before 40 h, the initial upper-level perturbation only slightly intensifies in the three model simulations, and the intensification rates are almost the same. Beyond 40 h, the cyclone in the CP grid model developed slightly more rapidly than that in L grid. The difference between the central surface pressures in these two calculations reaches about 5 hPa at 108 h. For Expt. 5, in which the grid distance is half of that in Expt. 1, the cyclone deepens faster than Expts. 1 and 4 after 40 h. The central surface pressure is about 930 hPa at 108 h, 5 hPa deeper than that in Expt. 1.

Similarly to Fig. 4b, Fig. 6b compares the exponential growth rates of the perturbation of the central surface pressure relative to 1000 hPa in Expts. 1, 4, and 5. The difference of the growth rates for these three experiments is negligible during the initial rapid growth period. Between 45 and 80 h, the growth rate in Expt. 4 is 7×10^{-6} s^{-1}, slightly smaller than that in Expt. 1. The growth rate in Expt. 5, between 40 and 70 h, is 9×10^{-6} s^{-1}, the largest one in these three experiments. It is obvious that the different model settings have effects on the normal mode growth rate, but the differences are on the order of 1×10^{-6} s^{-1}.

To compare with the forecast error growth arising from initial condition uncertainties, Fig. 7 shows the forecast errors (ΔP) arising from model uncertainties in Expts. 4 and 5 in terms of the central surface pressure difference relative to that in Expt. 1. The errors start with zero amplitude and remain close to zero until about 16 h into the integration. The errors reach

maxima of 10 hPa at 90 h for Expt. 5, and 6 hPa at 105 h for Expt. 4. In contrast to the initial condition error growth, there is no early rapid growth period for the model error growth. It is the aim of this research to characterize the rate of growth of the forecast errors that arise from model uncertainties. Unlike for the growth of forecast errors from initial condition uncertainty, there is no established theory for the time evolution of model uncertainty errors. It is clear from Fig. 7 that the initial growth of the forecast error cannot be represented by an exponential growth from an initial error, not least because the initial error (or difference between two model forecasts) is by definition zero. We assume that the model error growth is of the following form:

$$\Delta P(t) = \Delta P(t_1)\left(\frac{t}{t_1}\right)^{\mu}, \quad 0 < t < t_1, \tag{13}$$

where t_1 is the integrating time after initialization, at which the forecast errors start to grow exponentially, μ is the power of the time t elapsed during the forecast, and ΔP is the absolute value of the difference of the minimum central surface pressure between two forecasts, with different model configurations.

For Expt. 4, the value of t_1 is determined from a plot of the exponential growth rate of ΔP (Fig. 8b), which shows the exponential growth rate of ΔP starting from 16 h, before which the ΔP is close to zero. To determine the period over which there is exponential growth in Fig. 8b, we first calculate $\varepsilon(t)$ by

$$\varepsilon(t) = \frac{|\lambda(t) - \bar{\lambda}|}{|\bar{\lambda}|}, \tag{14}$$

where $\bar{\lambda}$ is averaged every 12 h. The exponential growth period is chosen when the criteria, $\varepsilon(t) \leq 0.5$, is satisfied. Consequently the value for t_1 is about 60 h, at which time the exponential growth rate has no strong oscillations and can be taken to be approximately constant (after 75 h the growth rate decreases, suggesting saturation). With $t_1 = 60$ h, the best fitting value of μ is found to be 3.1 (when the variance is minimum). Figure 8a is a plot of the forecast difference in terms of minimum central surface pressure relative to the control experiment along with the power law function of Eq. (13) with $\mu = 3.1$ and $t_1 = 60$ h. For the given parameters, Eq. (13) fits the data well until 60 h. Beyond 60 h, the error growth can be characterized as being close to an exponential normal mode growth phase (Fig. 8b), followed shortly afterwards by a saturation period as in the case of forecast error growth arising from initial condition uncertainties. The growth rate of ΔP is about 1.5×10^{-5} s^{-1} during the normal mode growth phase, bigger than that of the error growth rate in Expts. 2 and 3.

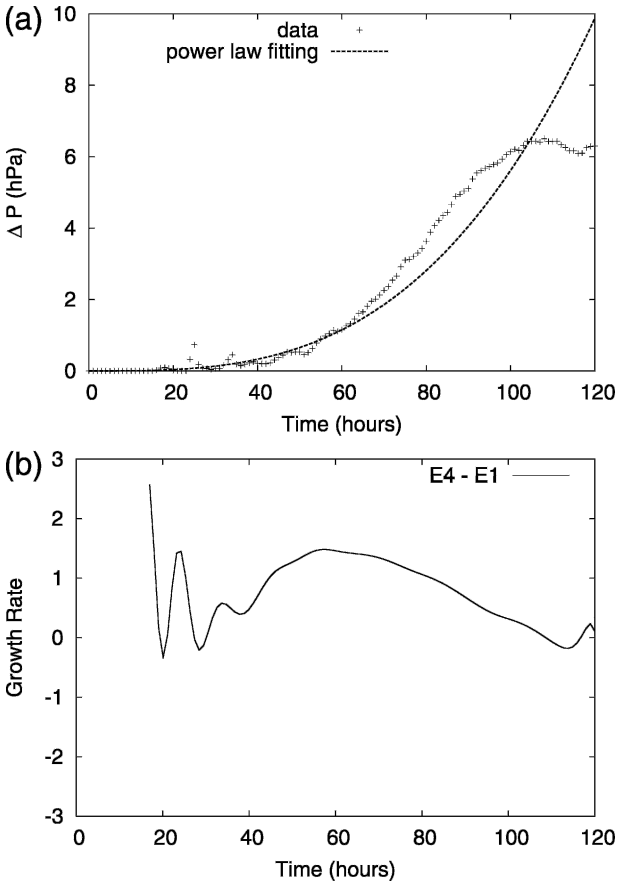

FIG. 8. Expt. 4: (a) plot of model error measured by central surface pressure (ΔP). Also shown is the function of Eq. (13) with $\mu = 3.1$ and $t_1 = 60$ h. (b) Exponential growth rate ($\times 10^{-5}$ s^{-1}) of the model error in terms of the minimum central surface pressure.

Similar to Fig. 8, Fig. 9 shows the forecast error growth for Expt. 5 measured by the minimum central surface pressure. The same analysis was done to determine values of t_1 and μ. During the first 55 h, the model error in Expt. 5 grows as t^3. Afterward, the model error grows exponentially at the growth rate of 1.7×10^{-5} s^{-1}. This is followed by a mature saturation period starting at 80 h.

Therefore, for forecast error caused by the model uncertainties, after a certain time, the error grows exponentially as for the initial condition uncertainties. One possible explanation is that the forecast error associated with model uncertainties, after a reasonable time interval, leads to errors, which will then proceed to grow as they would have if they had been present initially.

To generalize the difference of the forecast error growth resulting from initial condition and model un-

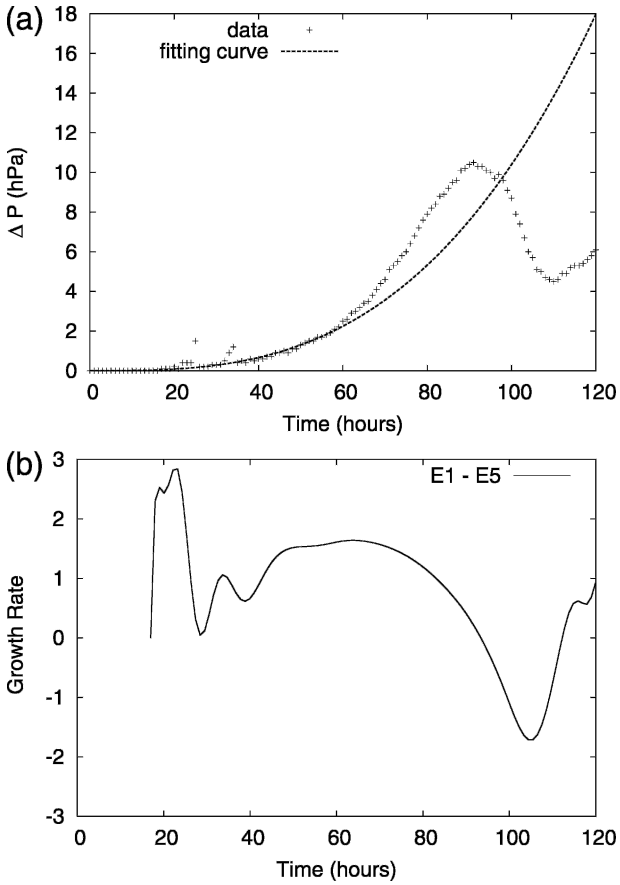

FIG. 9. Expt. 5: (a) plot of model error measured by the central surface pressure (ΔP). Also shown is the function of Eq. (13) with $\mu = 3.0$ and $t_1 = 55$ h. (b) Exponential growth rate ($\times 10^{-5}$ s^{-1}) of the model error in terms of the central surface pressure.

certainties in terms of the perturbation of the central surface pressure relative to the control experiment, the characteristics of the three different growing phases for Expts. 2, 3, 4, and 5 are listed in Table 2.

Table 2 shows that there are three phases for the forecast error growth in the experiments with initial condition (Expts. 2 and 3) and model uncertainties (Expts. 4 and 5). For the experiments with the structured initial condition uncertainties, the forecast errors grow rapidly at early transient times, with the growth rate well above the fastest growing normal mode. Afterward the error grows exponentially at approximately the same growth rate as the cyclone, and error growth rate then decreases in the mature period. For the experiments with the model uncertainties, the forecast errors are zero initially and slowly increase as a function of time to a power of ~3, later, an exponential growth phase starts with the growth rates being about twice of those in the initial error experiments. Finally, the error growth rates decrease as the cyclone reaches its mature stage. From the above comparison, we hypothesize that no matter whether the error originated from the initial condition or model uncertainties, after a certain time, the forecast errors grow exponentially, followed by a saturation period.

c. *Dependence of model uncertainty growth on initial amplitude of the cyclone*

Instead of starting with the initial condition in which the basic atmosphere is a zonal steady flow, we repeat the experiments with a flow that already contains developed cyclones, which is more representative of the numerical weather prediction process. To initialize the cyclone with different amplitudes, we randomly choose the model outputs of Expt. 1 at the integrating hours of 12, 20, 36, 42, 54, 63, 72, and 84, when the minimum central cyclone surface pressure perturbations (δP) relative to 1000 hPa are 6.0, 6.4, 10.5, 12.4, 17.4, 22.5, 29.1, and 40.8 hPa, respectively, as new initial conditions to repeat Expts. 1 and 4. For the control experiment, the minimum surface pressure perturbation (δP) relative to 1000 hPa is initially about 2.7 hPa. Thus the new two groups of experiments begin with more intense initial cyclones than those in Expts. 1 and 4. We name the Expts. 1 and 4 with the new initial conditions as Expt. 1′ and Expt. 4′, respectively, to distinguish them from the original experiments.

As an example, Fig. 10 shows the difference in terms of the minimum surface pressure between Expts. 1′ and 4′ using the 72-h model output from Expt. 1 as the starting condition for the model simulations. In contrast to Fig. 7, in Fig. 10 the forecast error associated with the model uncertainty grows more rapidly at the early integrating hours instead of slowly increasing. Using the same method as for Figs. 8 and 9, we find that before 8

TABLE 2. Comparison of forecast error growth for initial condition and model uncertainties

Expt.	Phase 1	Phase 2	Phase 3
2	Initial rapid growth	Exponential growth, $45 > t > 75$, $\lambda = 0.8 \times 10^{-5}$ s^{-1}	Saturation
3	Initial rapid growth	Exponential growth, $45 > t > 80$, $\lambda = 0.9 \times 10^{-5}$ s^{-1}	Saturation
4	$\delta P(t_1)(t/t_1)^{\mu}$, $\mu = 3.1$, $t_1 = 60$, $t < t_1$	Exponential growth, $60 > t > 75$, $\lambda = 1.5 \times 10^{-5}$ s^{-1}	Saturation
5	$\delta P(t_1)(t/t_1)^{\mu}$, $\mu = 3.0$, $t_1 = 55$, $t < t_1$	Exponential growth, $55 > t > 80$, $\lambda = 1.7 \times 10^{-5}$ s^{-1}	Saturation

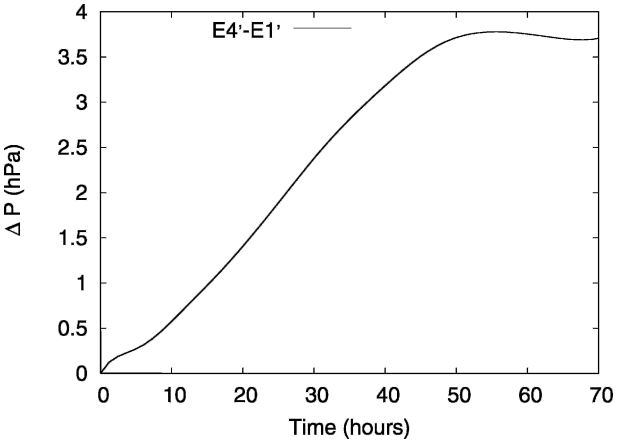

FIG. 10. The central surface pressure difference between Expts. 4′ and 1′ using start data from Expt. 1 at 72 h.

h, the forecast error grows as the square root of time (see Fig. 11a). After 8 h, the error growth is approximately exponentially with the growth rate of 2.3×10^{-5} s^{-1}, after 15 h followed by a saturation period (see Fig. 11b). Because the simulation started with a relatively strong cyclone, the exponential growth period is rather short in this experiment, about 7 h. It is possible that forecast errors associated with model uncertainties only experience growth periods of phase 1 and phase 3 when the initial cyclone perturbation (δP) is large enough; for example, a mature cyclone. A square root of time dependence for the model error growth was also found by Orrell et al. (2001), who compared the ECMWF operational model forecast relative to the verifying analysis. This kind of anomalously rapid initial error growth is also discussed by Lorenz (1995).

To understand the relationship of the strength of the initial cyclone with the values of t_1 and μ in Eq. (13), Fig. 12 plots the values of μ and t_1 in Eq. (13) versus the values of the initial cyclone central surface pressure perturbation relative to 1000 hPa (δP) in Expt. 4′. Starting an integration with a stronger initial cyclone, here is a shorter time, t_1, needed to reach the exponential growth and saturation periods. Consistent with this is a smaller value of μ. For example, when the initial central pressure perturbation (δP) is bigger than 16 hPa (a stronger initial cyclone), the forecast error grows as time to a power, μ, smaller than 1, and t_1 is less than 20 h. For the simulations with the initial cyclone central surface pressure perturbation (δP) smaller than 6 hPa (a weaker initial cyclone), the forecast error grows as time to third power, and t_1 is bigger than 50 h. A similar comparison for the value of the forecast error (ΔP) in terms of the central surface pressure at the time t_1 is plotted in Fig. 12b. It shows that for a weaker initial cyclone (δP smaller than 10 hPa), the exponential error growth starts when the forecast error (ΔP) reaches about 1.5 hPa; with a stronger cyclone (δP bigger than 17 hPa), the exponential error growth starts when the forecast error (ΔP) is only about 0.5 hPa.

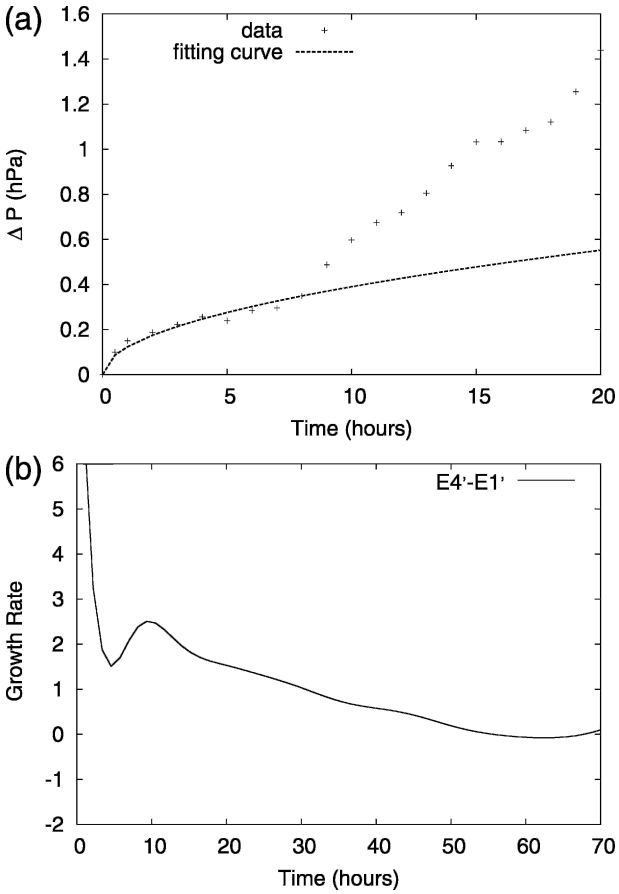

FIG. 11. Expt. 4′ using starting data from Expt. 1 at 72 h: (a) plot of model error measured by central surface pressure perturbation relative to Expt. 1′. Also shown is the function of Eq. (13) with $\mu = 0.5$ and $t_1 = 8$ h. (b) Growth rate of the model error measured by the central surface pressure difference between Expts. 4′ and 1′.

d. Spatial pattern of forecast error

To investigate the forecast error propagation associated with the initial condition uncertainty, the differences between the surface pressure of Expts. 2 and 1 are compared in the left panel of Fig. 13. At the starting time (not shown), the surface pressure difference between the two experiments is about 0.5 hPa and the scale of the perturbation is about 500 km. After day 1 (Fig. 13a), the central cyclone surface pressure difference reaches 1 hPa, and the scale of the perturbation also increases to 1000 km. At day 3 (Fig. 13c), the primary cyclone central surface pressure difference is

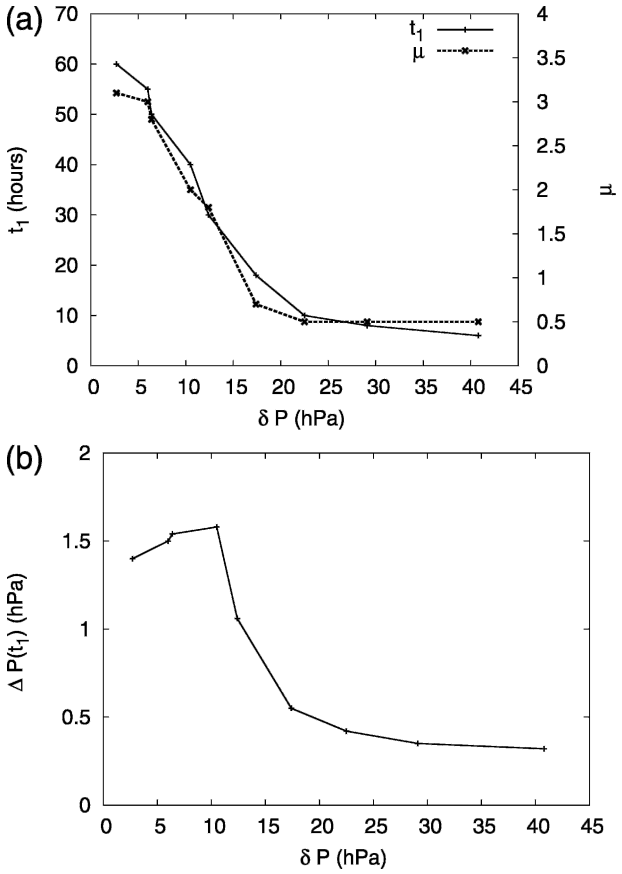

FIG. 12. (a) The values of t_1 and μ, and (b) forecast error in terms of the difference of the central surface pressure (ΔP) at the time $t = t_1$, are plotted against the initial cyclone central surface pressure perturbation relative to 1000 hPa (δP) in Expt. 4′.

about 6 hPa and the perturbation grows to a scale comparable to the size of the cyclone. Meanwhile the forecast errors propagate eastwards with the primary cyclone. Errors also propagate downstream and upstream accompanying the upstream and downstream cyclone development. At day 5 (Fig. 13e), the forecast errors associated with the primary cyclone are mainly located in the regions of the warm and cold fronts, and in the central region of the primary cyclone. It is clear that the forecast errors not only grow through a baroclinic process, but also propagate with the wave dispersion.

Similar to the left panel of Fig. 13, the right panel of Fig. 13 compares the differences between the surface pressures of Expts. 4 and 1 to study the forecast error growth associated with the model uncertainties. For Expt. 4, the initial errors are zero at the beginning, and the surface pressure differences remain small at day 1 (Fig. 13b). After day 3, the surface pressure perturbation reaches 3 hPa and propagates eastward with a comparable scale to the primary cyclone (Fig. 13d). Downstream and upstream propagation (Figs. 13d,f) are also observed as for the initial condition uncertainties. After day 5, the errors in the primary cyclone are similar in strength for Figs. 13e,f, but model uncertainty gives much larger errors for the upstream and downstream cyclones. The forecast error growth associated with the upstream and downstream cyclones development is a subject for our future studies.

e. Other measures of forecast error growth

As well as the central surface pressure, other attributes of the developing cyclone have been used to measure the forecast error growth. The behavior of the forecast error growth associated with the initial condition and the model uncertainties are very similar to the results discussed above when the maximum surface vorticity is chosen as a measure. We have also investigated the forecast error growth in terms of the volume-integrated kinetic energy of the primary cyclone. Apart from the fact that the exponential growth rates [and μ value in Eq. (13)] are about double those calculated when using the minimum central surface pressure difference, the three phases of forecast error growth for Expts. 2, 3, 4, and 5 are consistent with Table 2, which is what we would expect.

Figure 14 compares the track errors for Expts. 2, 3, 4, and 5. We have defined the cyclone center using a quadratic interpolator (Smith et al. 1990). The track errors increase only slowly and remain less than one grid length of the model until about 60 h. During this period, the cyclones mainly move eastwards. After 60 h, when the exponential cyclone growth starts, the cyclones begin to move northeastwards. Because of the different intensities of the primary cyclone, the speeds of northward movement are different, and track errors begin to increase more rapidly.

4. Discussion and summaries

Loss of predictability occurs not only because of inevitable uncertainty in initial conditions, but also because of the inevitable uncertainties in our ability to represent computationally the governing equations of weather and climate. From the numerical weather prediction forecast system alone, we cannot separate out the effects of model and initial condition uncertainties, since they are convoluted in the assimilation cycle. Our aim in this paper is to use an empirical method to compare the forecast error growth originating from the initial condition and the model uncertainties, and also to construct a theoretical basis for describing model-uncertainty-based forecast error growth.

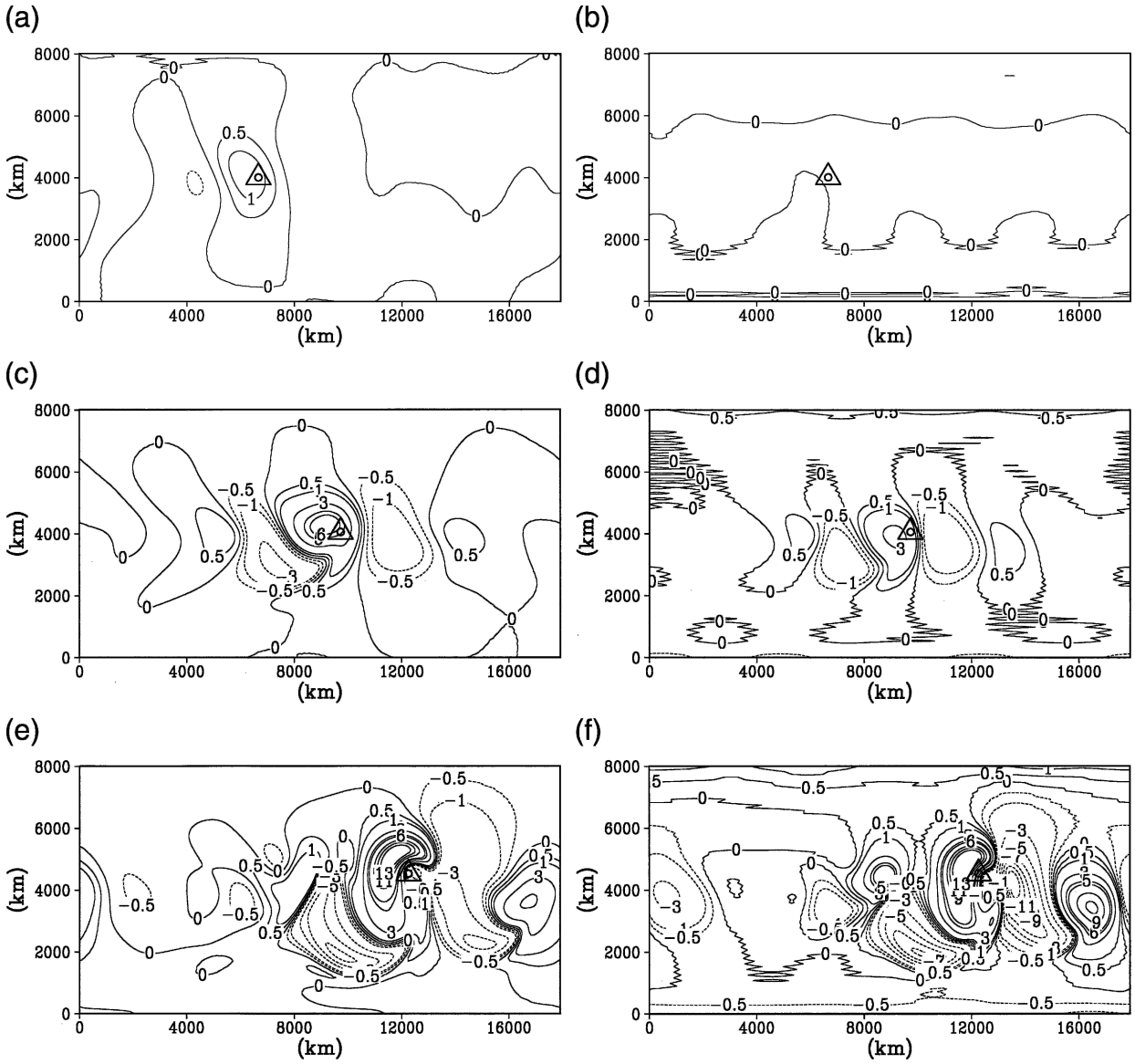

FIG. 13. (left) Forecast error in terms of the difference of surface pressure between Expts. 2 and 1 after (a) day 1, (c) day 3, (e) day 5. (right) Forecast error in terms of the difference of surface pressure between Expts. 4 and 1 after (b) day 1, (d) day 3, (f) day 5. The triangle symbol represents the surface cyclone center of the control experiment.

Both the cyclone and forecast error associated with the initial uncertainties have three growth phases: an early initial phase of transient growth, with the growth rate well above that of the most unstable normal mode, an exponential growth phase and a saturation phase. The exponential growth rates of the cyclone and the forecast error associated with the initial uncertainties are similar. This shows that over the lifetime of a cyclone it is important to have accurate initial conditions to be able to forecast cyclone development with some skill. If it had been the case that error growth was much faster than that of cyclone itself, then existing such initial condition error would prevent skillful forecasts from being possible.

For the experiments with model uncertainties, the forecast errors are initially zero and increase as time to a power of μ, where μ is in the range from $\sim$0.5 to $\sim$3, depending on the intensity of the initial cyclone. After a certain time, the model errors grow exponentially, followed by a saturation period. Starting an integration with a stronger initial cyclone, the cyclone takes a shorter time to reach the exponential growth period and the initial forecast error growth associated with the model uncertainty grows more rapidly at early times

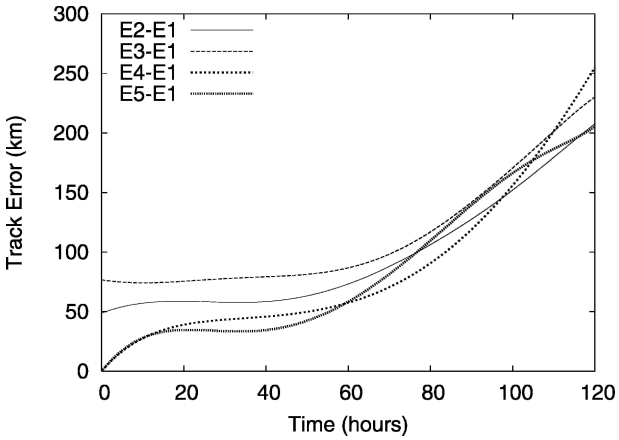

FIG. 14. The distance (km) between the center of the primary cyclone in Expt. 1 and that in Expts. 2, 3, 4, and 5, respectively.

with a smaller μ value. Also when the initial cyclone is strong enough, then the exponential growth phase may only last for a very short time. A dynamical interpretation for the growth of forecast errors resulting from model uncertainties is the subject of ongoing research.

Forecast errors not only grow through baroclinic processes, but also propagate with the same speed as the primary cyclone. In terms of the surface pressure, the forecast error grows upscale, and also propagates upstream and downstream accompanying the upstream and downstream cyclone development.

In future research these results will be extended to model perturbations resulting from different physical parameterization schemes, parameters within a scheme and the inclusion of stochastic physics. It is also our future interests to investigate the growth of initial condition and model uncertainties associated with the upstream and downstream cyclone development. We aim to develop an empirical model of the functional dependence on time of the forecast spread, resulting from model uncertainties.

Acknowledgments. We are grateful to Dr. Fuqing Zhang and Dr. Rich Rotunno for providing the code for the initialization, and to Dr. Chris Snyder and two anonymous reviewers for their useful comments and critique. We would also like to thank Dr. Robert Plant for helpful discussions and for his thoughtful comments on an earlier version of this paper. This work was funded by Natural Environment Research Council (NERC) in the United Kingdom.

REFERENCES

Arakawa, A., 1972: Design of the UCLA general circulation model: Numerical simulation of weather and climate. Tech. Rep. 7, Dept. of Meteorology, University of California, Los Angeles, 116 pp.

——, and V. Lamb, 1977: Computational design of the basic dynamical processes of the UCLA general circulation model. *Methods in Computational Physics,* Vol. 17, J. Chang, Ed., Academic Press, 173–265.

——, and M. J. Suarez, 1983: Vertical differencing of the primitive equations in sigma coordinates. *Mon. Wea. Rev.,* **111,** 34–45.

——, and S. Moorthi, 1988: Baroclinic instability in vertically discrete systems. *J. Atmos. Sci.,* **45,** 1688–1707.

——, and C. S. Konor, 1996: Vertical differencing of the primitive equations based on the Charney-Phillips grid in hybrid $\sigma - p$ vertical coordinates. *Mon. Wea. Rev.,* **124,** 511–528.

Badger, J., and B. Hoskins, 2001: Simple initial value problems and mechanisms for baroclinic growth. *J. Atmos. Sci.,* **58,** 38–49.

Buizza, R., J. Barkmeijer, T. Palmer, and D. Richardson, 1999: Current status and future developments of the ECMWF ensemble prediction system. *Meteor. Appl.,* **6,** 1–14.

Charney, J. G., and N. A. Phillips, 1953: Numerical integration of the quasi-geostrophic equations for barotropic and simple baroclinic flows. *J. Meteor.,* **10,** 71–99.

Cullen, M. J. P., T. Davies, M. H. Mawson, J. A. James, S. C. Coulter, and A. Malcolm, 1997: An overview of numerical methods for the next generation U.K. NWP and climate model. *Numerical Methods in Atmospheric and Ocean Modelling: The Andre J. Robert Memorial Volume,* C. A. Lin, R. Laprise, and H. Ritchie, Eds., Canadian Meteorological and Oceanographic Society, 425–444.

Davis, C. A., and K. A. Emanuel, 1991: Potential vorticity diagnosis of cyclogenesis. *Mon. Wea. Rev.,* **119,** 1929–1952.

Downton, R. A., and R. S. Bell, 1988: The impact of analysis differences on a medium-range forecast. *Meteor. Mag.,* **117,** 279–285.

Eady, E. T., 1949: Long waves and cyclone waves. *Tellus,* **1,** 33–52.

Farrell, B. F., 1982: The initial growth of disturbances in a baroclinic flow. *J. Atmos. Sci.,* **39,** 1663–1686.

——, 1984: Modal and non-modal baroclinic waves. *J. Atmos. Sci.,* **41,** 1663–1686.

Harrison, M. S. J., T. Palmer, D. S. Richardson, and R. Buizza, 1999: Analysis and model dependencies in medium-range ensembles: Two transplant case studies. *Quart. J. Roy. Meteor. Soc.,* **125,** 2487–2515.

Hollingsworth, A., 1995: A spurious mode in the "Lorenz" arrangement of ϕ and T which does not exist in the "Charney-Phillips" arrangement. ECMWF Tech. Memo. 211, 12 pp.

Lorenz, E. N., 1960: Energy and numerical weather prediction. *Tellus,* **12,** 364–373.

——, 1963: Deterministic nonperiodic flow. *J. Atmos. Sci.,* **20,** 130–141.

——, 1989: Effects of analysis and model errors on routine weather forecasts. *Proc. ECMWF Seminars on Ten Years of Medium-Range Weather Forecasting,* Reading, United Kingdom, ECMWF, 115–128.

——, 1995: Predictability—A problem partly solved. *Proc. ECMWF Seminars on Predictability,* Reading, United Kingdom, ECMWF, 1–18.

Molteni, F., R. Buizza, T. N. Palmer, and T. Petroliagis, 1996: The new ECMWF ensemble prediction system: Methodology and validation. *Quart. J. Roy. Meteor. Soc.,* **122,** 73–119.

Nicolis, C., 2003: Dynamics of model error: Some generic features. *J. Atmos. Sci.,* **60,** 2208–2218.

Orrell, D., L. Smith, J. Barkmeijer, and T. Palmer, 2001: Model

error in weather forecasting. *Nonlinear Processes Geophys.,* **9,** 357–371.

Palmer, T., 1999: A nonlinear dynamical perspective on climate prediction. *J. Climate,* **12,** 575–591.

——, 2000: Predicting uncertainty in forecasts of weather and climate. *Reports on Progress in Physics,* Vol. 63, Institute of Physics Publishing, 71–116.

Rotunno, R., and J. Bao, 1996: A case study of cyclogenesis using a model hierarchy. *Mon. Wea. Rev.,* **124,** 1051–1066.

——, W. C. Skamarock, and C. Snyder, 1994: An analysis of frontogenesis in numerical simulations of baroclinic waves. *J. Atmos. Sci.,* **51,** 3373–3398.

Richardson, D. S., 1997: The relative effect of model and analysis differences on ECMWF and UKMO operational forecasts. *Proc. ECMWF Workshop on Predictability,* Reading, United Kingdom, ECMWF, 363–372.

Simmons, A. J., and D. M. Burridge, 1981: An energy- and angular-momentum-conserving vertical finite-difference scheme and hybrid vertical coordinates. *Mon. Wea. Rev.,* **109,** 758–766.

Smith, R., W. Ulrich, and G. Dietachmaye, 1990: A numerical study of tropical cyclone motion using a barotropic model. Part I. The role of vortex asymmetries. *Quart. J. Roy. Meteor. Soc.,* **116,** 337–362.

Snyder, C., T. Hamill, and S. Trier, 2003: Linear evolution of error covariances in a quasigeostrophic model. *Mon. Wea. Rev.,* **131,** 189–205.

Takayabu, I., 1991: "Coupling development": An efficient mechanism for the development of extra-tropical cyclones. *J. Meteor. Soc. Japan,* **69,** 609–628.

Tan, Z., F. Zhang, R. Rotunno, and C. Snyder, 2004: Mesoscale predictability of moist baroclinic waves: Experiments with parameterized convection. *J. Atmos. Sci.,* **61,** 1794–1804.

Thompson, P., 1957: Uncertainty of initial state as a factor in the predictability of large scale atmospheric flow patterns. *Tellus,* **9,** 275–295.

Tokioka, T., 1978: Some consideration on vertical differencing. *J. Meteor. Soc. Japan,* **56,** 89–111.

Toth, Z., and E. Kalnay, 1993: Ensemble forecasting at NMC: The generation of perturbations. *Bull. Amer. Meteor. Soc.,* **74,** 2317–2330.

Vannitsem, S., and Z. Toth, 2002: Short-term dynamics of model errors. *J. Atmos. Sci.,* **59,** 2594–2604.

Wernli, H., R. Fehlmann, and D. Luethi, 1998: The effect of barotropic shear on upper-level induced cyclogenesis: Semigeostrophic and primitive equation numerical simulations. *J. Atmos. Sci.,* **55,** 2080–2094.

Zhu, H., and R. K. Smith, 2003: Effects of vertical differencing in a minimal hurricane model. *Quart. J. Roy. Meteor. Soc.,* **129,** 1051–1069.

——, ——, and W. Ulrich, 2001: A minimal three-dimensional tropical cyclone model. *J. Atmos. Sci.,* **58,** 1924–1944.